Experimental and numerical analysis of buoyancy-induced instability during CO_2 absorption in $NaHCO_3$-Na_2CO_3 aqueous solutions

C. Wylock*[,a], A. Rednikov[a], P. Colinet[a], B. Haut[a]

[a] *Transfers, Interfaces and Processes, Université Libre de Bruxelles, 50 av. F.D. Roosevelt CP 165/67, 1050 Brussels, Belgium*

Abstract

This work deals with the experimental analysis and the mathematical modelling of the CO_2 absorption in an initially quiescent aqueous solution of $NaHCO_3$ and Na_2CO_3 inside a Hele-Shaw cell. This absorption, initially driven by the coupling between diffusion and chemical reactions, eventually leads to the apparition of a peculiar gravitational instability with non-monotonic dynamics, and liquid plumes generated at some distance from the gas-liquid interface (Wylock et al., 2014). Considering that this instability is triggered by a Rayleigh-Taylor like mechanism, a two-dimensional model, coupling diffusion, chemical reaction and convection, is proposed to simulate the onset and the dynamics of such an instability. It is observed that the simulated instability dynamics agree qualitatively with the experimental observation and that the order of magnitude of the onset time is well estimated. Thanks to the simulation, the interaction between the various phenomena after the instability onset is further investigated and a mechanism is proposed to explain the unusual dynamics of the studied system. It is notably shown that this dynamics is due to the particular non-monotonic density variations with the depth, induced by the absorption. A criterion to obtain such type of density profile is presented. In addition, the simulation enables to assess the influence of the instability on the CO_2 absorption rate and it is observed that the generated flow pattern does not lead to a significant enhancement of the gas-liquid absorption rate. This result is of significant importance for

*Corresponding author
Email address: cwylock@ulb.ac.be (C. Wylock)

Preprint submitted to Chemical Engineering Science

optimizing chemisorption (e.g. for CO_2 capture or sequestration) processes.

Key words: gas-liquid absorption, chemical reactions, mathematical modelling, Hele-Shaw cell, Rayleigh-Taylor instability

1. Introduction

Numerous chemical engineering operations are based on the absorption of a gaseous component into a liquid phase. It is commonly admitted that the global gas-liquid mass transfer rate in these operations is controlled by phenomena occurring in layers close to the gas-liquid interface (Bird et al., 2002; Coulson and Richardson, 1999; Danckwerts, 1970; Trambouze and Euzen, 2004), such as the diffusive transport of the involved species and the chemical reactions. A good understanding of these phenomena is thus of fundamental interest for the modelling of these operations.

Recently, the carbon dioxide (CO_2) absorption in aqueous alkaline solutions inside a Hele-Shaw cell became more and more studied in the framework of the CO_2 sequestration in deep saline aquifers (Loodts et al., 2014a,b; Javaheri et al., 2010; Kim and Choi, 2012; Kim, 2015; Riaz et al., 2006; Rongy et al., 2012; Wylock et al., 2008, 2011, 2013, 2014). Using these Hele-Shaw cells, many of these studies have indeed highlighted the occurrence of a Rayleigh-Taylor (RT) instability when CO_2 is absorbed in alkaline solutions, resulting from an unstable liquid density stratification during the absorption. Indeed, the chemical reactions involving CO_2 that take place in such solutions may modify locally the liquid density in the reaction zone, leading to the appearance of natural convection when heavier liquid lies upon lighter liquid.

The parallel between CO_2 absorption in a liquid in a Hele-Shaw cell and CO_2 sequestration in porous media such as saline aquifers lies in the fact that the only possible mixing mechanism to add up to the effect of chemical reactions in enhancing the CO_2 transfer is buoyancy-induced convection. The analysis of RT instability taking place in a Hele-Shaw cell is therefore of significant importance for further development of CO_2 sequestration processes, especially in order to identify the conditions favoring the overall transfer efficiency.

In previous works, a Hele-Shaw cell has been used to investigate the CO_2 absorption in aqueous solutions of sodium bicarbonate ($NaHCO_3$) and carbonate (Na_2CO_3) (Wylock et al., 2008, 2011). This absorption is indeed

met in several industrial processes (e.g. Solvay process for refined $NaHCO_3$ production) and it is an interesting model to analyze the CO_2 absorption in saline aquifers. Using a Mach-Zehnder interferometer (MZI, see sketch in Fig. 2), the local density variations (DV) resulting from the CO_2 absorption in the liquid are visualized thanks to the refractive index (RI) variations caused by the DV. Full details of this device and of the associated image processing is given in Wylock et al. (2011).

During experiments, the appearance of RT instability has been systematically observed (see the video's in supplementary material). A typical time evolution of the DV field is presented in Fig. 1. During the first stage of absorption, the DV field is homogeneous on any horizontal line. At this stage, the absorption is controlled only by diffusion and reaction. The DV appears to be negative at the gas-liquid interface and to present a positive maximum at some distance from the interface (as illustrated in Fig. 4). After some time, the onset of a RT instability is observed. Some plumes are generated at a small distance from the interface and fall towards the bottom of the cell. These plumes may sometimes show an oscillating behavior (as in Fig. 1). In such cases, it is observed that the plumes tend to slow down at some depth, soften, and almost vanish. Meanwhile, a second generation of plumes appears in between the primary ones, and the same scenario is possibly repeated several times. In other cases, the plumes do not vanish when they sink but the location of their origin is varying.

The dynamics of the RT instability observed in this system is rather unusual. Indeed, most of the referenced RT instabilities occurring during acid-base reactions correspond to plumes originating at the fluid interface, and penetrating the bulk without any oscillating behavior. Therefore, their effect on the overall gas-liquid mass transfer may be significantly different from those of a classical RT instability.

The objectives of this work are therefore:

- to develop a mathematical model of the transport phenomena taking place in a Hele Shaw cell during the absorption of CO_2 in an initially quiescent liquid, considering a generic chemical reaction $CO_2 + \nu_B B \rightarrow \nu_C C$ in the liquid phase, without any particular assumption on its reaction rate (contrary to what we have done for instance in Wylock et al. (2014));

- to use direct numerical simulations of this model and the experimental results obtained using the MZI device to get further insight into the

This is the preprint version of a manuscript accepted in Chemical Engineering Science
Permalink: http://dx.doi.org/10.1016/j.ces.2016.04.061

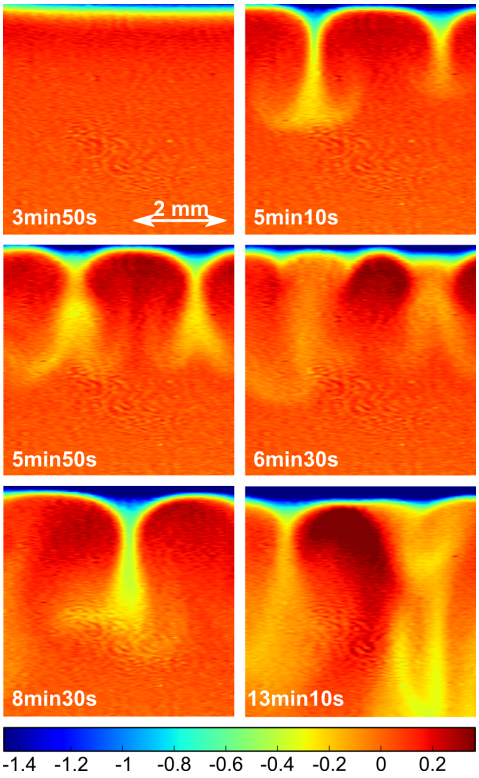

Fig. 1: DV fields (in kg/m^3, see colorbar below) obtained at different times during the CO_2 absorption in an aqueous solution of 789 mol/m^3 of $NaHCO_3$ and 625 mol/m^3 of Na_2CO_3 (case 18, see Table 1). The instability development is highlighted on these images. These images were obtained experimentally using the MZI.

dynamics of the particular RT instability observed in this work, when CO_2 is absorbed in an initially quiescent aqueous aqueous $NaHCO_3$ and Na_2CO_3 liquid solution.

2. Absorption experiments

The gas-liquid CO_2 absorption in an aqueous solution of $NaHCO_3$ and Na_2CO_3 has been realized in a Hele-Shaw cell made of two flat plates (5 cm x 10 cm) of polymethylmethacrylate, placed in a MZI. A sketch of this cell and the MZI device is presented in Fig. 2. The solution is introduced in the cell by its bottom and fills partially the gap between the plates. The absorption in the stagnant liquid is triggered by forcing gaseous CO_2 to flow along over the liquid thanks to the particular shape of the spacer between

This is the preprint version of a manuscript accepted in Chemical Engineering Science
Permalink: http://dx.doi.org/10.1016/j.ces.2016.04.061

the two plates, with an obstacle between the gas inlet and outlet, to ensure a homogeneous and constant CO_2 partial pressure in the gaseous phase above the interface. As early mentioned, full details of the experimental setup can be obtained in Wylock et al. (2011).

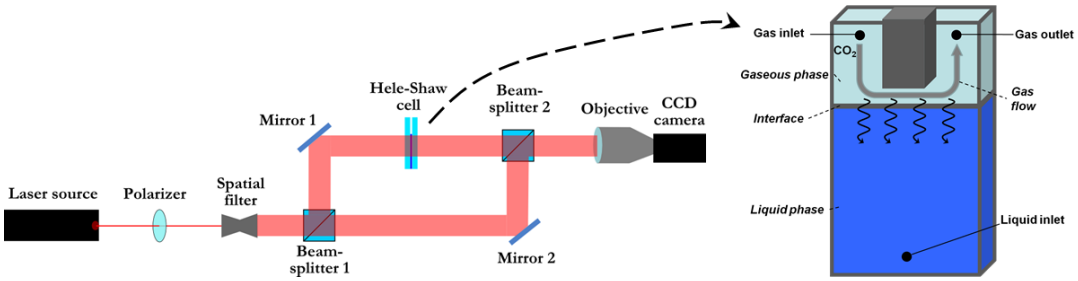

Fig. 2: Sketch of the MZI device and of the Hele-Shaw cell.

All the absorption experiments were realized at a temperature T=298.15 K. The gaseous CO_2 was saturated with water vapor prior to its entrance in the cell, with a total pressure 101325 Pa, leading to a CO_2 partial pressure of p_{CO_2}=99293 Pa. The distance between the plates of the Hele-Shaw cell, which corresponds to the thickness of the liquid in the direction perpendicular to the plates, was measured using a calliper rule to be $e = 1.9\,10^{-3}$ m.

A set of CO_2 absorption experiments, using several couples of $NaHCO_3$-Na_2CO_3 initial concentrations, were realized. A case number has been assigned to each couple, as it is presented in Table 1. Hereafter, an experiment and its corresponding simulation are identified by their case number.

In each experiment, as soon as the gaseous CO_2 flow was initiated, images were recorded every 2 s. These images were converted into liquid DV fields which were then analyzed. Before the instability onset, the DV field is almost homogeneous in any horizontal line. Therefore, at a given time, the DV field can be horizontally averaged in a window to draw a plot of the liquid DV versus the distance from the interface (called hereafter the DV profile at this time).

The time of the instability onset was estimated visually from the DV field time evolution. It corresponds to the time when the DV field starts to become inhomogeneous in some horizontal lines.

This is the preprint version of a manuscript accepted in Chemical Engineering Science
Permalink: http://dx.doi.org/10.1016/j.ces.2016.04.061

N°	$[Na_2CO_3]_0$ $\left(\frac{mol}{m^3}\right)$	$[NaHCO_3]_0$ $\left(\frac{mol}{m^3}\right)$
1	195	246
2	398	251
3	609	256
4	828	261
5	1055	266
6	1290	271
7	1534	276
8	1786	282
9	198	499
10	404	509
11	617	519
12	839	529
13	1068	539
14	1036	549
15	1552	559
16	201	760
17	409	774
18	625	789

Table 1: Case number of the analyzed couples of initial $NaHCO_3$ and Na_2CO_3 concentrations.

3. Mathematical modelling and numerical simulation

3.1. Computational domain and variables

A two-dimensional approach is followed in order to develop a mathematical model of the CO_2 gas-liquid transfer in a Hele-Shaw cell. In this model, only the phenomena taking place in the liquid phase are considered. A two-dimensional cartesian coordinate system (x, y) is defined, where x and y are the horizontal and vertical coordinates (parallel to the plates), respectively. The computational domain is a rectangle extending from $x = -w/2$ to $x = w/2$ and from $y = -d$ to $y = 0$. w and d denotes the width and the depth of the domain (m), respectively. It is worth to mention that the potential effect of the meniscus shape on the mass transport in the liquid has been estimated in Wylock et al. (2011), by numerical simulation of a mass transport model coupling diffusion and reaction, in a two-dimensional do-

This is the preprint version of a manuscript accepted in Chemical Engineering Science
Permalink: http://dx.doi.org/10.1016/j.ces.2016.04.061

main corresponding to the vertical cross-section of the cell (i.e. in the plane perpendicular to the plates). It has been concluded that the liquid phase in the meniscus region is quickly saturated, i.e. the concentration fields are homogeneous in this region. Regarding the mass transfer, the complex meniscus can hence be seen as a simple flat interface, horizontal and located at the bottom of the meniscus.

A sketch of the domain is presented in Fig. 3. The gas-liquid interface is located at $y = 0$, while the bottom of the computational domain is located at $y = -d$. The so-called lateral boundaries are located at $x = -w/2$ and $x = w/2$.

The other variables defined as follows. t is the time (s), u and v are the horizontal and the vertical components of the velocity (m/s), respectively, and p is the pressure (in Pa). The concentration of a species X is written $[X]$ (mol/m^3).

3.2. Chemical reaction

The mathematical model is developed considering that the CO_2 absorbed in the solution reacts irreversibly with a component B (i.e. the reactant) to form a component C (i.e. the reaction product):

$$CO_2 + \nu_B\, B \rightarrow \nu_C\, C \tag{1}$$

where ν_B and ν_C are the stoichiometric coefficients of B and C, respectively. The reaction rate is noted r (mol/m^{3}s) and its expression depends on the considered chemical system. The model can be used for any chemical system which can be described by Eq. (1).

In the case of the CO_2 - $NaHCO_3$ - Na_2CO_3 system, the actual chemical reactions are reversible and follow a reaction scheme with two successive reactions. However, as clearly detailed in Appendix A.1, the characteristics of this system are such that the global reaction is well described by Eq. (1). Indeed, on the one hand, the equilibrium constant of the reaction with CO_2 has a value such that, at equilibrium, the CO_2 concentration is negligible compared to the CO_3^{2-} and HCO_3^- concentrations. On the other hand, the equilibrium constant of the other reaction is such that B and C stand for CO_3^{2-} and HCO_3^-, respectively, with $\nu_B = 1$ and $\nu_C = 2$ (see Eq. (41) in Appendix A.1). The resulting expression of r for the global reaction is given by Eq. (42) (also in Appendix A.1).

This is the preprint version of a manuscript accepted in Chemical Engineering Science
Permalink: http://dx.doi.org/10.1016/j.ces.2016.04.061

3.3. Species transport

Assuming that the diffusive transports can be modelled by the Fick's law and ignoring cross-diffusion effects, species balances lead to the following mass transport-reaction equations:

$$\frac{\partial[\mathrm{CO_2}]}{\partial t} + u\frac{\partial[\mathrm{CO_2}]}{\partial x} + v\frac{\partial[\mathrm{CO_2}]}{\partial y} = D_{\mathrm{CO_2}}\left(\frac{\partial^2[\mathrm{CO_2}]}{\partial x^2} + \frac{\partial^2[\mathrm{CO_2}]}{\partial y^2}\right) - r \quad (2)$$

$$\frac{\partial[B]}{\partial t} + u\frac{\partial[B]}{\partial x} + v\frac{\partial[B]}{\partial y} = D_B\left(\frac{\partial^2[B]}{\partial x^2} + \frac{\partial^2[B]}{\partial y^2}\right) - \nu_B r \quad (3)$$

$$\frac{\partial[C]}{\partial t} + u\frac{\partial[C]}{\partial x} + v\frac{\partial[C]}{\partial y} = D_C\left(\frac{\partial^2[C]}{\partial x^2} + \frac{\partial^2[C]}{\partial y^2}\right) + \nu_C r \quad (4)$$

where $D_{\mathrm{CO_2}}$, D_B and D_C are the diffusion coefficients ($\mathrm{m^2/s}$) of $\mathrm{CO_2}$, B and C, respectively.

At time $t = 0$, the concentrations are considered homogeneous in the liquid filling the cell. The initial conditions write:

$$[\mathrm{CO_2}]|_{x,\,y,\,t=0} = 0 \quad (5)$$

$$[B]|_{x,\,y,\,t=0} = [B]_0 \quad (6)$$

$$[C]|_{x,\,y,\,t=0} = [C]_0 \quad (7)$$

where $[B]_0$ and $[C]_0$ are the initial concentrations of B and C, respectively.

At the interface ($y = 0$), the $\mathrm{CO_2}$ concentration in the liquid phase is assumed to be instantaneously at equilibrium with the gaseous phase (Harvey and Smith, 1959). Considering that B and C do not pass through the interface, no-flux conditions are used for these species. Since $v = 0$ at the interface (see Eq. (27)), the no-flux condition reduces to a condition of zero diffusive flux across this interface. Therefore, the boundary conditions at the interface read:

$$[\mathrm{CO_2}]|_{x,\,y=0,\,t} = h_{\mathrm{CO_2}}\frac{p_{\mathrm{CO_2}}}{RT} \quad (8)$$

$$-D_B\left.\frac{\partial[B]}{\partial y}\right|_{x,\,y=0,\,t} = 0 \quad (9)$$

$$-D_C\left.\frac{\partial[C]}{\partial y}\right|_{x,\,y=0,\,t} = 0 \quad (10)$$

where $h_{\mathrm{CO_2}}$ is the $\mathrm{CO_2}$ solubility coefficient (dimensionless), $p_{\mathrm{CO_2}}$ (Pa) is the $\mathrm{CO_2}$ partial pressure in the gaseous phase (considered homogeneous), R is the ideal gas constant and T is the absolute temperature of the liquid.

This is the preprint version of a manuscript accepted in Chemical Engineering Science
Permalink: http://dx.doi.org/10.1016/j.ces.2016.04.061

Since the computational domain is not as deep as the real cell, it is considered that its bottom ($y = -d$) is an open boundary with no normal diffusive flux:

$$\left.\frac{\partial[\mathrm{CO_2}]}{\partial y}\right|_{x,\, y=-d,\, t} = 0 \tag{11}$$

$$\left.\frac{\partial[B]}{\partial y}\right|_{x,\, y=-d,\, t} = 0 \tag{12}$$

$$\left.\frac{\partial[C]}{\partial y}\right|_{x,\, y=-d,\, t} = 0 \tag{13}$$

In order to mimic a cell without lateral wall (i.e. a cell with an infinite width), periodic boundary conditions are set on the lateral boundaries. They write:

$$[\mathrm{CO_2}]|_{x=-\frac{w}{2},\, y,\, t} = [\mathrm{CO_2}]|_{x=\frac{w}{2},\, y,\, t} \tag{14}$$

$$[B]|_{x=-\frac{w}{2},\, y,\, t} = [B]|_{x=\frac{w}{2},\, y,\, t} \tag{15}$$

$$[C]|_{x=-\frac{w}{2},\, y,\, t} = [C]|_{x=\frac{w}{2},\, y,\, t} \tag{16}$$

3.4. Momentum transport and continuity

Describing the three-dimensional flow in a Hele-Shaw cell using a two-dimensional approach requires averaging the Navier-Stokes equation across the cell gap. In this paper, the Navier-Stokes-Darcy (NSD) approach is used, assuming a parabolic Poiseuille like profile across the gap, such as in Gondret and Rabaud (1997); Martin et al. (2002); Wylock et al. (2008). In this case, the NSD equation differ from the classical Navier-Stokes equation by the presence of the so-called Darcy term as well as by a coefficient 6/5 multiplying the advective term. Despite not being completely rigorous beyond the Darcy domain (Ruyer-Quil, 2001), it is shown in Martin et al. (2002) that the NSD equation is appropriate for the kind of problem treated here. Since the liquid DV resulting from the gas-liquid CO_2 transfer are approximately three order of magnitude smaller than the liquid initial density (Wylock et al., 2011), the Boussinesq approximation is implied (i.e. the effect of the DV on the flow field is taken into account only in the volume force term).

Based on these assumptions, the momentum and continuity equations

This is the preprint version of a manuscript accepted in Chemical Engineering Science
Permalink: http://dx.doi.org/10.1016/j.ces.2016.04.061

read:

$$\rho\left(\frac{\partial u}{\partial t}+\frac{6}{5}\left(u\frac{\partial u}{\partial x}+v\frac{\partial u}{\partial y}\right)\right)+\frac{12\,\mu}{e^2}u = -\frac{\partial p}{\partial x}+\mu\left(\frac{\partial^2 u}{\partial x^2}+\frac{\partial^2 u}{\partial y^2}\right) \quad (17)$$

$$\rho\left(\frac{\partial v}{\partial t}+\frac{6}{5}\left(u\frac{\partial v}{\partial x}+v\frac{\partial v}{\partial y}\right)\right)+\frac{12\,\mu}{e^2}v = -\frac{\partial p}{\partial y}+\mu\left(\frac{\partial^2 v}{\partial x^2}+\frac{\partial^2 v}{\partial y^2}\right) - \Delta\rho g \quad (18)$$

$$\frac{\partial u}{\partial x}+\frac{\partial v}{\partial y} = 0 \quad (19)$$

where ρ is the liquid density (kg/m^3), μ is the liquid dynamic viscosity (kg/(m s)), e is the distance between the plates of the Hele Shaw cell (m) and g is the gravity acceleration (m/s^2). ρ and μ depends on the given initial mixture composition but they are considered constant during the absorption process.

It is considered that the liquid density variation $\Delta\rho$ (kg/m^3) is due to the B and C concentration variations induced by the CO_2 absorption. In this work, it is considered that $\Delta\rho$ depends linearly of the concentration variations:

$$\Delta\rho|_{x,\,y,\,t} = \left.\frac{\partial\rho}{\partial[B]}\right|_{[B]_0,[C]_0}\Delta[B]|_{x,\,y,\,t}+\left.\frac{\partial\rho}{\partial[C]}\right|_{[B]_0,[C]_0}\Delta[C]|_{x,\,y,\,t} \quad (20)$$

$\frac{\partial\rho}{\partial[B]}$ and $\frac{\partial\rho}{\partial[C]}$ (in kg/mol) are the partial derivatives of the density with respect to the B and C concentrations, respectively. $\Delta[B]|_{x,\,y,\,t}$ and $\Delta[C]|_{x,\,y,\,t}$ are given by:

$$\Delta[B]|_{x,\,y,\,t} = \Big([B]|_{x,\,y,\,t}-[B]_0\Big) \quad (21)$$

$$\Delta[C]|_{x,\,y,\,t} = \Big([C]|_{x,\,y,\,t}-[C]_0\Big) \quad (22)$$

It has been shown in Wylock et al. (2011) that such a relation can be written in the case of the absorption of CO_2 in an aqueous solution of $NaHCO_3$ and Na_2CO_3, as detailed in Appendix A.1. Nevertheless, it is worth to mention that it is not crucial to use a linear relation between the concentrations and the DV under the form of Eq. (20). Any other relation can be numerically implemented in the model.

This is the preprint version of a manuscript accepted in Chemical Engineering Science
Permalink: http://dx.doi.org/10.1016/j.ces.2016.04.061

Initially, it is assumed that the liquid is quiescent and that the excess pressure field equals zero:

$$u|_{x,\,y,\,t=0} = 0 \quad (23)$$
$$v|_{x,\,y,\,t=0} = 0 \quad (24)$$
$$p|_{x,\,y,\,t=0} = 0 \quad (25)$$

A slip boundary condition is used at the interface ($y = 0$): there is no shear stress and the vertical velocity equals zero. These conditions read:

$$\left.\frac{\partial u}{\partial y}\right|_{x,\,y=0,\,t} + \left.\frac{\partial v}{\partial x}\right|_{x,\,y=0,\,t} = 0 \quad (26)$$
$$v|_{x,\,y=0,\,t} = 0 \quad (27)$$

As it is considered that the computational domain bottom is an open boundary, the following no stress condition is used at $y = -d$:

$$\mu\left(\left.\frac{\partial u}{\partial y}\right|_{x,\,y=-d,\,t} + \left.\frac{\partial v}{\partial x}\right|_{x,\,y=-d,\,t}\right) = 0 \quad (28)$$
$$-p|_{x,\,y=-d,\,t} + 2\mu\left.\frac{\partial v}{\partial y}\right|_{x,\,y=-d,\,t} = 0 \quad (29)$$

As for the mass transport, periodic boundary conditions are set on the lateral boundaries for the velocity and pressure fields. They read:

$$u|_{x=-\frac{w}{2},\,y,\,t} = u|_{x=\frac{w}{2},\,y,\,t} \quad (30)$$
$$v|_{x=-\frac{w}{2},\,y,\,t} = v|_{x=\frac{w}{2},\,y,\,t} \quad (31)$$
$$p|_{x=-\frac{w}{2},\,y,\,t} = p|_{x=\frac{w}{2},\,y,\,t} \quad (32)$$

The physico-chemical parameters appearing in the model are given in Appendix A.2, for the case of CO_2 absorption in aqueous solutions of $NaHCO_3$ and Na_2CO_3 inside a Hele-Shaw cell.

3.5. Numerical procedure

To simulate the evolution of the system during the CO_2 absorption in the liquid, Eqs. (2)-(4) and (17)-(19) have to be solved simultaneously using the initial conditions (5)-(7) and (23)-(25), the boundary conditions (8)-(16)

This is the preprint version of a manuscript accepted in Chemical Engineering Science
Permalink: http://dx.doi.org/10.1016/j.ces.2016.04.061

and (26)-(32) and with Eq. (20) to compute the DV field. This transient boundary-value problem is solved numerically using finite elements, with the commercial software COMSOL Multiphysics 5.0.

Since the experimental view frame was a 7 mm x 7 mm window, the computational domain is selected as a square with $w = d = 10$ mm. A mapped mesh is used to discretize the equations. The horizontal boundaries (interface and bottom) are preliminary meshed with 50 node points regularly spaced. On the vertical lateral boundaries, 100 node points are placed, such that the distance between two successive points linearly increases with the decrease of y (i.e. when going towards the bottom of the cell) and such that the ratio of the distance between the two last points to the distance between the two first points is 20. Therefore, the mesh becomes gradually coarser when y decreases. A sketch of the meshed domain is presented in Fig. 3. The resulting mesh is made of 5000 rectangular elements. The thickness of the first element at the interface is $1.67\,10^{-5}$ m and its width is $2\,10^{-4}$ m.

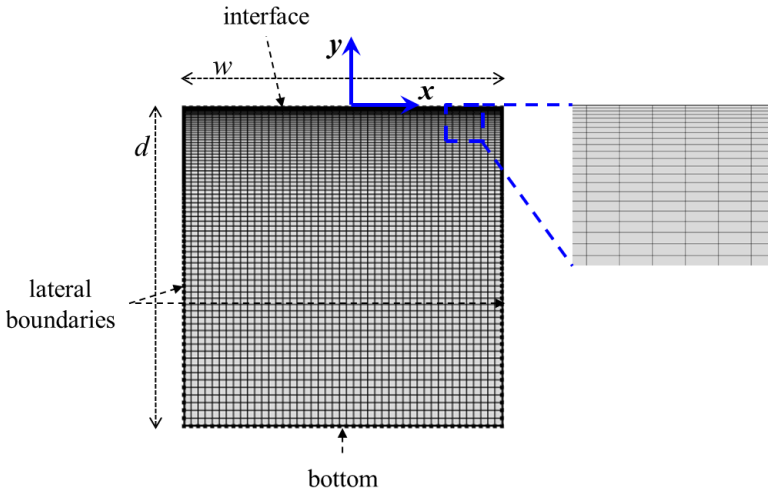

Fig. 3: Sketch of the meshed computational domain, with a zoom on a zone close to the interface.

The independence of the solution with respect to the mesh has been evaluated only before the onset of the instability. Indeed, due to the fact that the non-linear term in the NSD equation makes the system chaotic after the instability onset, any minor change between two simulation conditions may lead to different evolutions. Therefore, the mesh independence of the solution of the equations has not been evaluated after the instability onset.

This is the preprint version of a manuscript accepted in Chemical Engineering Science
Permalink: http://dx.doi.org/10.1016/j.ces.2016.04.061

All dependent variables ($[CO_2]$, $[B]$, $[C]$, u, v and p) are discretized using a quadratic Lagrangian element scheme. It is worth to mention that, very often, p is discretized with linear elements. However, it has been observed that this discretization order may be not enough, especially for observing phenomena like the oscillatory behavior. Due to the particular shape of the DV, a second order scheme has to be used for p. No noise is imposed on the variables to trigger the instability; it appears thanks to the numerical noise.

The direct solver MUMPS is used, with backward differentiation for the time stepping. The other solver parameters are left at their default values. The numerical convergence has been reached for all cases.

4. Results and discussions

4.1. Mechanism triggering the RT instability

In all the experiments, it is observed that the plumes resulting from the RT instability are created between 0.5 mm and 1 mm below the interface, as it is illustrated in Fig. 4, where two different cases are presented: Fig. 4-a corresponds to the case 2 and Fig. 4-b corresponds to the case 7. In Fig. 4, for each case, a DV field before and after the instability onset is presented. Additionally, for each case, some DV profiles are presented, at different times between the start of the experiment and just before the instability onset.

An examination of the DV profile before the instability onset highlights that it is non-monotonic (see Fig. 4). There are two distinct regions in the liquid inside the Hele-Shaw cell. At the interface, the DV is negative. Then the DV increases with the distance from the interface, becomes positive, reaches a maximum before finally decreasing smoothly to zero. The DV profile presents thus a maximum positive value at some distance from the interface.

Moreover, it is observed that the plumes are originating approximately from where this maximum DV is generated. Therefore, it can reasonably be assumed that the plumes originate at a small distance from the interface because their driving force - the maximum DV - is located at this distance from the interface.

Such a particular DV profile appears in the liquid because the reactant and the reaction product have different diffusivities and different contributions to the density. This can be understood thanks to the development of an analytical expression (see detailed development in Appendix B) describing the DV profile before the instability onset. This development is based on two

This is the preprint version of a manuscript accepted in Chemical Engineering Science
Permalink: http://dx.doi.org/10.1016/j.ces.2016.04.061

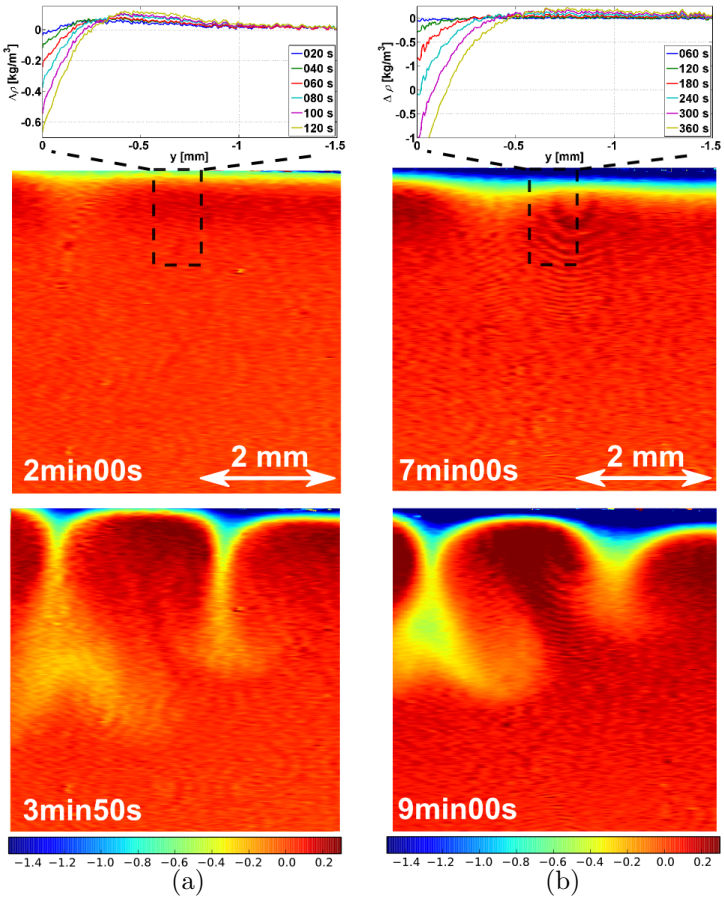

Fig. 4: Liquid DV profile and liquid DV field (in kg/m^3, see colorbar below) at different times during the absorption of CO_2 in aqueous solutions of $NaHCO_3$ and Na_2CO_3, for case 2 (a) and case 7 (b). These are experimental results.

main assumptions: the reaction takes place instantaneously at the interface and, before the instability onset, the only mass transport mechanism is diffusion along the vertical direction y. The rationale for the first assumption is the fact that the reaction characteristic time is much smaller than the diffusion characteristic times of A, B and C in the liquid. The second assumption is consistent with the experimental observation of the DV independent of x before the instability onset. According to these assumptions, an expression can be derived for the DV profile (see Appendix B). In dimensional form, it

This is the preprint version of a manuscript accepted in Chemical Engineering Science
Permalink: http://dx.doi.org/10.1016/j.ces.2016.04.061

writes:

$$\Delta\rho(t,y) = [B]_0 \left(\frac{\partial\rho}{\partial[C]} \frac{\nu_C}{\nu_B} \sqrt{\frac{D_B}{D_C}} \mathrm{erfc}\left(\frac{-y}{2\sqrt{D_C t}} \right) - \frac{\partial\rho}{\partial[B]} \mathrm{erfc}\left(\frac{-y}{2\sqrt{D_B t}} \right) \right) \tag{33}$$

From Eq. (33), it can be observed that $[B]_0$ determines the amplitude of the DV profile while $[C]_0$ has no influence on it. The shape of the DV profile is controlled by two ratios (see Appendix B): D_C/D_B and $\nu_C \frac{\partial\rho}{\partial[C]} / \nu_B \frac{\partial\rho}{\partial[B]}$. The particular DV profile observed experimentally is obtained when these two ratios satisfy the following conditions:

$$\frac{D_C}{D_B} > 1 \tag{34}$$

$$\frac{\nu_C \frac{\partial\rho}{\partial[C]}}{\nu_B \frac{\partial\rho}{\partial[B]}} < \sqrt{\frac{D_C}{D_B}} \tag{35}$$

It should be noted that a similar criterion, restricted to the case $\nu_B = \nu_C = 1$, has been presented in Wylock et al. (2014). Although the criterion presented in this paper can be rigorously applied only in the case of an instantaneous reaction taking place at the interface, it is worth to mention that it is verified in all the cases considered in this paper (this can be verified thanks to values presented in Table 1).

The experimental results can be compared to numerical simulation results. For this purpose, the equations of the model are first solved, using appropriate values of the physicochemical parameters, depending on the case considered (see Appendix A.2). Then, the time evolution of the numerically computed concentration fields is used to compute the time evolution of the density variation field $\Delta\rho^{\mathrm{sim}}(x,y,t)$ (thanks to Eq. (20)). The simulation results are presented in Fig. 5, for the cases 2 and 7. In this figure, the field of $\Delta\rho^{\mathrm{sim}}(x,y,t)$ is presented, for each case, before and after the instability onset. Moreover, the simulated DV profiles are presented, for each case, at some times before the instability onset.

It is observed in Fig. 5 that the simulated DV fields or profiles agree with the experimental ones before the instability onset. The simulated DV is negative at the interface, it increases with the depth in the liquid, becomes positive with a maximum at some distance from the interface and then finally decreases smoothly to zero. In the simulations, the plumes are also triggered at some distance from the interface, close to where the maximum DV is located.

This is the preprint version of a manuscript accepted in Chemical Engineering Science
Permalink: http://dx.doi.org/10.1016/j.ces.2016.04.061

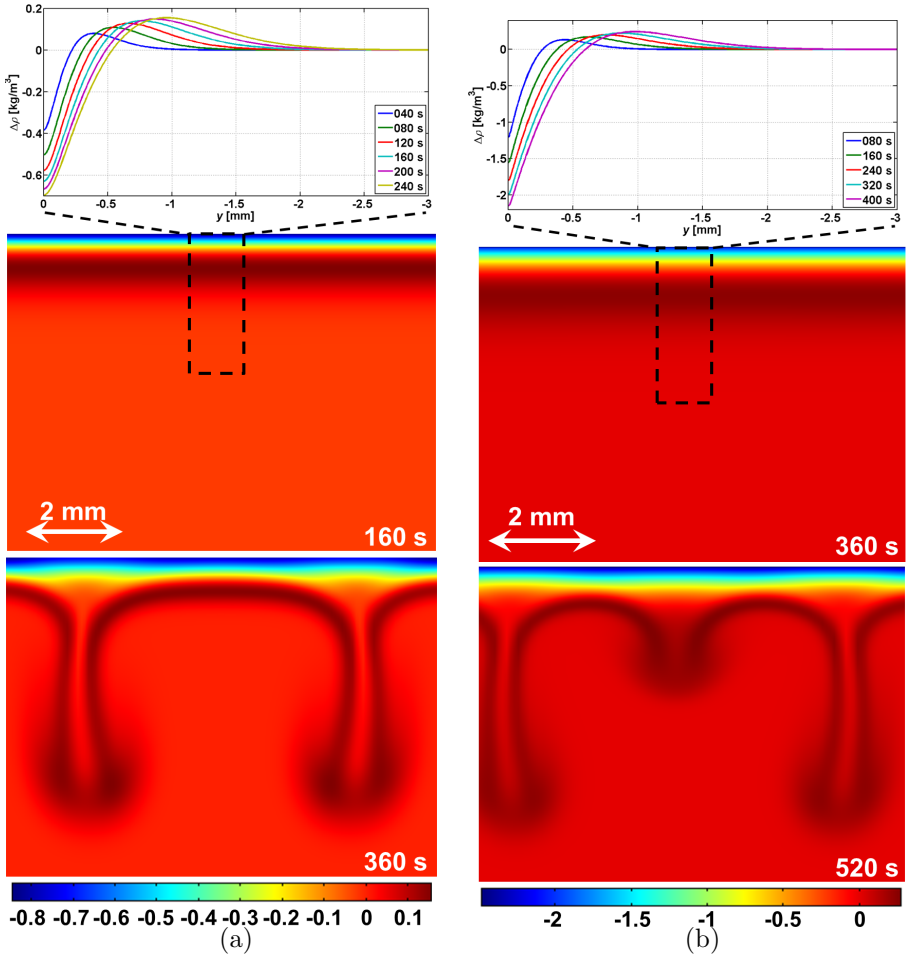

Fig. 5: Liquid DV profile and liquid DV field (in kg/m^3, see colorbar below) at different times during the absorption of CO_2 in aqueous solutions of $NaHCO_3$ and Na_2CO_3, for case 2 (a) and case 7 (b). These are simulation results.

4.2. Characteristics of the instability onset

The instability onset is analyzed over the whole experimental set in terms of the onset time (written $t_{\text{onset}}^{\text{exp}}$) and of the driving force for the instability (written $p_{\text{onset}}^{\text{exp}}$). As mentioned in Section 2, $t_{\text{onset}}^{\text{exp}}$ is estimated visually from the DV field time evolution. Concerning the instability driving force, it is here assumed that it corresponds to the hydrostatic pressure exerted by the bump in the DV profile just before the onset. This pressure is noted $p_{\text{onset}}^{\text{exp}}$ and it is calculated by the integral of the positive part of the DV profile

This is the preprint version of a manuscript accepted in Chemical Engineering Science
Permalink: http://dx.doi.org/10.1016/j.ces.2016.04.061

$p^{\mathrm{exp}}_{\mathrm{onset}} = g \int_{\Delta\rho(y)>0} \Delta\rho(y)\, dy$.

For each experiment, the equations of the model are solved using the corresponding values of the initial concentrations and physicochemical parameters (see Tables 1 and 2). Then, the onset time ($t^{\mathrm{sim}}_{\mathrm{onset}}$) and the instability driving force ($p^{\mathrm{sim}}_{\mathrm{onset}}$) are calculated from the determined velocity and concentration fields. $p^{\mathrm{sim}}_{\mathrm{onset}}$ is calculated as for an experiment, while $t^{\mathrm{sim}}_{\mathrm{onset}}$ is the time when the simulated velocity field starts showing velocity vectors with an amplitude larger than 10^{-5} m/s. Indeed, it has been observed that, when such a threshold is exceeded, the simulated DV field becomes significantly heterogeneous in some horizontal lines.

$t^{\mathrm{exp}}_{\mathrm{onset}}$, $p^{\mathrm{exp}}_{\mathrm{onset}}$, $t^{\mathrm{sim}}_{\mathrm{onset}}$ and $p^{\mathrm{exp}}_{\mathrm{onset}}$ are presented in Fig. 6. Experimental data are represented by triangle up and the simulated results by triangle down. For each point, the corresponding case number is displayed. The onset time is plotted versus the driving force for the instability in Fig. 6-a and versus the total initial concentration $[Na_2CO_3]_0 + [NaHCO_3]_0$ in Fig. 6-b. It is observed that the simulated and experimental data have the same order of magnitude, although there is a significant scatter, indicating that t_{onset} is not fully correlated to p_{onset} or to the total concentration. Yet, the variability among the various cases is moderate regarding the onset time. It can also be observed in Fig. 6-a that the simulation results regarding p_{onset} are globally larger than the experimental results.

However, trends seem to emerge in Fig. 6-a and 6-b, especially regarding the experimental data. $t^{\mathrm{exp}}_{\mathrm{onset}}$ tends to increase with $p^{\mathrm{exp}}_{\mathrm{onset}}$ and with $[Na_2CO_3]_0 + [NaHCO_3]_0$, respectively. A possible explanation for this observation is that the instability onset is strongly influenced by the liquid viscosity, which increases with the initial total concentration. If the viscosity increases, the instability needs an increased driving force induced by the bump in the DV profile, and this driving force needs thus a longer time to be developed.

This trend is also shown by the simulation results, although $p^{\mathrm{sim}}_{\mathrm{onset}}$ is almost systematically overestimated, when compared to the experimental data. Such discrepancies may come from the procedure to estimate the pressure related to the bump (in DV profiles), especially from the experimental results. Indeed, these latter are noisy compared to the smooth profiles generated in simulations, as it can be noticed when one compares the profiles presented in Figs. 4 and 5. The fluctuations observed in the experimentally obtained DV profiles may reduce the value estimated through the profile integration.

This is the preprint version of a manuscript accepted in Chemical Engineering Science
Permalink: http://dx.doi.org/10.1016/j.ces.2016.04.061

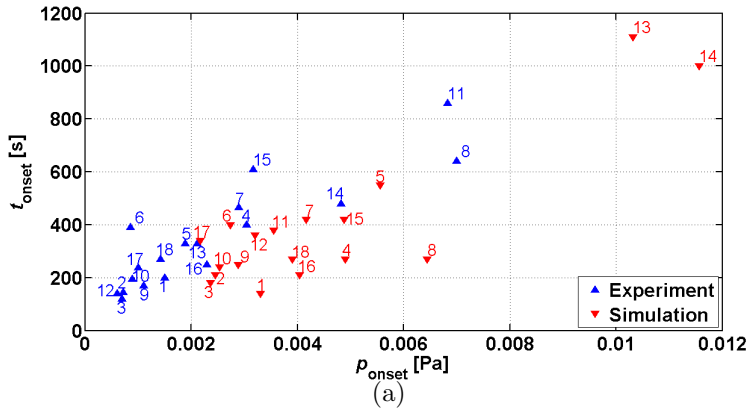

(a)

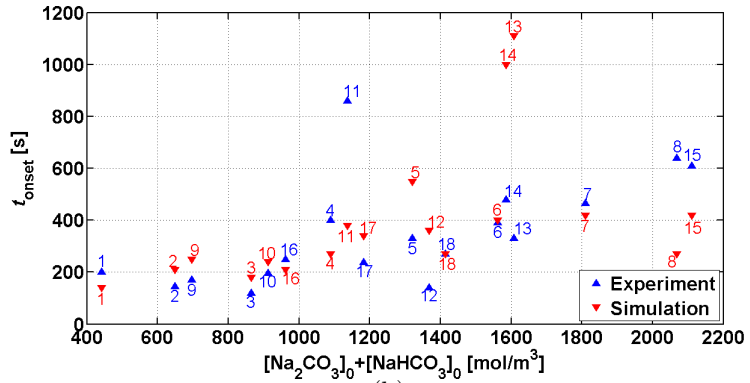

(b)

Fig. 6: Time of the instability onset versus the instability driving force (a) and versus the total concentration (b): experimental (triangle up) and numerical results (triangle down). The marker label identifies the corresponding case.

Another possibility to consider is that the two-dimensional model presented in this paper (which uses the NSD formalism) in not realistic enough to include all the phenomena inducing the Rayleigh-Taylor instability in the used Hele-Shaw cell. Besides, in this cell, the free interface between the gas and the liquid has a meniscus shape, which is ignored in the two-dimensional model. It should then be useful to develop and simulate a three-dimensional model, taking into account the meniscus shape of the gas-liquid interface, to compare with the results of the two-dimensional model and with the experimental results.

This is the preprint version of a manuscript accepted in Chemical Engineering Science
Permalink: http://dx.doi.org/10.1016/j.ces.2016.04.061

4.3. Dynamics of the system after the instability onset

The experimentally and numerically determined DV fields can be analyzed in order to gain insight into the dynamics of the system after the instability onset.

The experimental results show that, once they have appeared, the plumes may slide to the right or to the left, as illustrated in Fig. 7 for the case 2 (see also the corresponding video in supplementary material), or even exhibit in some cases an oscillating behavior, as observed in Fig. 1 for the case 18. In this latter case, it is observed that after the onset (at approximately 4 min 30 s), the formed plumes tend to slow down while they reach a depth of about 2.5 mm (5 min 50 s), soften, and almost vanish (6 min 30 s). Then, a second generation of plumes appears in between the primary ones (8 min 30 s), repeating the same sequence a second and last time (13 min 10 s). As shown in Fig. 8, this plume dynamics is qualitatively reproduced by the numerical simulations, at least shortly term after their onset. However, it is worth to mention that the long term evolution of the simulated plumes can differ from the experimental ones. The real plumes evolve in a domain wider than 1 cm, while the simulation are realized in a two-dimensional domain with periodic boundary conditions at the lateral boundaries. It is therefore not surprising to observe discrepancies when convection motion has appeared, which may indeed be significantly influenced by such differences between the real and the numerical domain.

Besides, once the instability has started, the experimental results show that the liquid layer located between the interface and the depth where the plumes are generated has a DV that does not depend on the horizontal direction. Hence, it can be assumed that this liquid is almost stagnant (see Figs. 1 and 7). This is confirmed by the simulation results (see below). This can be explained by the fact that, in this layer of liquid, the DV increases with an increase of the distance from the interface. Hence, the stratification is stable and not much affected by convection.

The existence of this stagnant liquid layer is clearly shown by an examination of the numerically simulated velocity fields after the instability onset, as presented in Fig. 9 for the case 18. In this figure, the color represents the velocity modulus $\sqrt{u^2 + v^2}$ and the arrows the velocity vectors. Two distinct liquid zones can be observed on this figure. At a distance from the interface larger than 0.5 mm, in what we call the mixing zone, the liquid velocity is high (of the order of 0.1 mm/s). In the liquid layer between the interface and where the plumes are generated, the liquid velocity is much smaller (between

This is the preprint version of a manuscript accepted in Chemical Engineering Science
Permalink: http://dx.doi.org/10.1016/j.ces.2016.04.061

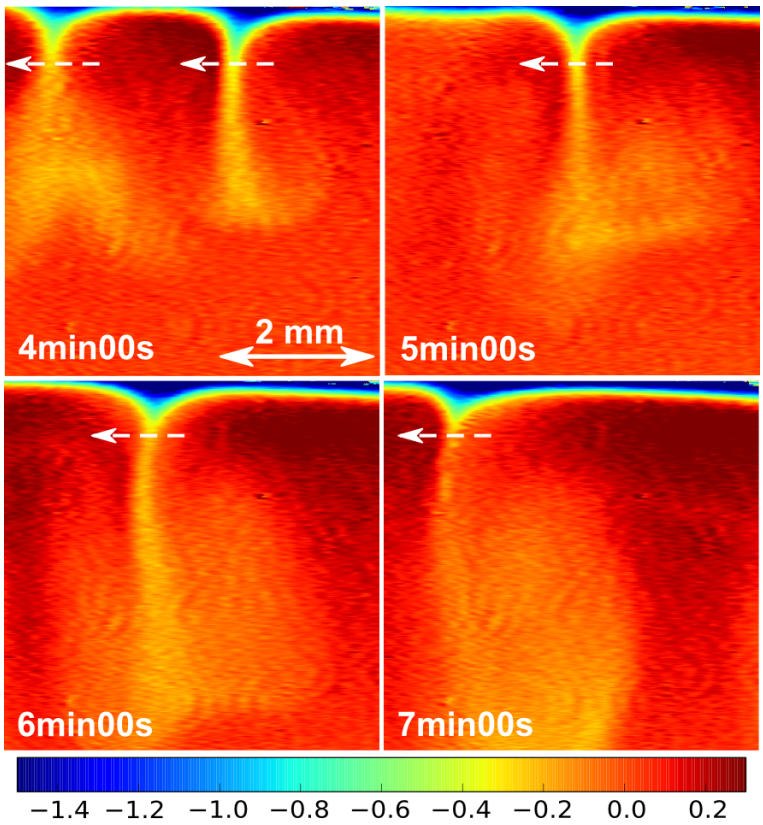

Fig. 7: Time evolution of the liquid DV field (in kg/m^3, see colorbar below) for case 2, after the instability onset. The sliding of the plumes is indicated by arrows. Note the low density zone near the interface (stagnant zone), which is rather horizontally homogeneous, despite convection plumes

1 and 10 μm/s). Hereafter, this zone is therefore called the stagnant liquid layer. It is worth to mention that this distance of 0.5 mm from the interface corresponds approximately to the zone where $\Delta\rho < 0$. The stagnant layer therefore corresponds to the zone where the DV stratification is stable.

The numerical simulations can be analyzed in order to propose a mechanism to explain the occasionally observed oscillating behavior of the plumes. In Fig. 10, a simulated DV field is presented, for case 18, after the instability onset but before the second generation of plumes. The diffusive fluxes of B and C (dashed lines) and their convective fluxes (solid lines) are also sketched in this figure. Finally, in the inset, the DV along two vertical lines (one along a plume and one between two plumes) is also presented.

This is the preprint version of a manuscript accepted in Chemical Engineering Science
Permalink: http://dx.doi.org/10.1016/j.ces.2016.04.061

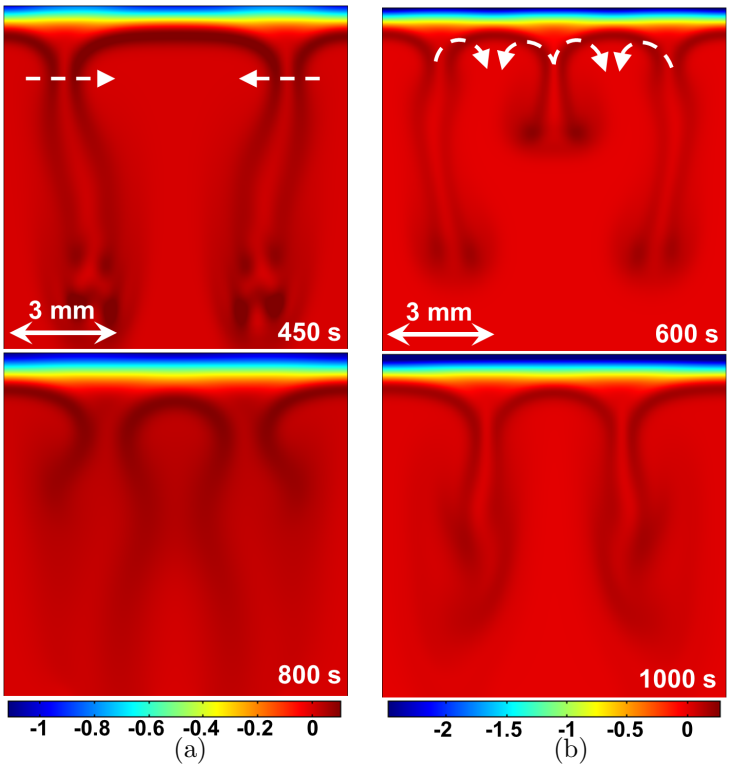

Fig. 8: Simulated liquid DV field (in kg/m^3, see colorbar below) at different times during the absorption of CO_2 in aqueous solutions of $NaHCO_3$ and Na_2CO_3, illustrating sliding plumes for case 2 (a) and oscillating plumes for case 7 (b).

In Fig. 10, it is observed that, after the instability onset, the DV along the vertical straight line between plumes presents a maximum. This is not the case for the DV along the vertical line along the plumes. The most unstable region is therefore located between the previously formed plumes. This discrepancy in the DV profiles between two locations is likely to result from the combined action of the diffusive and convective transports.

On the one hand, the simulation shows that the respective upward and downward diffusive fluxes of B and C in the stagnant layer are slightly enhanced by the convection in the region just above the zone where the liquid flows upward. Indeed, the conveyed upward liquid is richer in fresh reactant B and poorer in C than in the stagnant layer. The diffusive fluxes in the stagnant zone are thus enhanced by this vertical flow in the mixed zone.

This is the preprint version of a manuscript accepted in Chemical Engineering Science
Permalink: http://dx.doi.org/10.1016/j.ces.2016.04.061

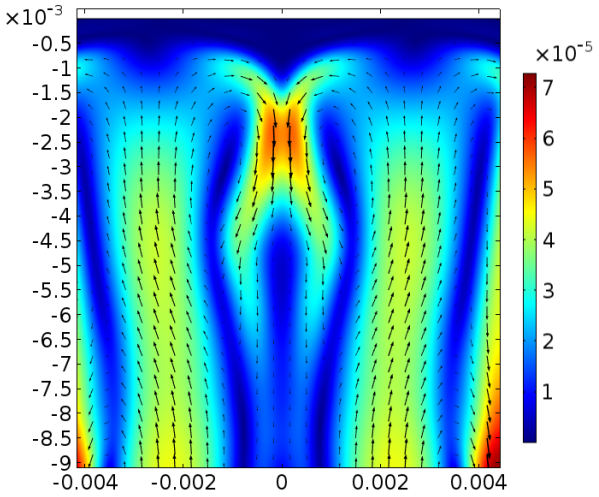

Fig. 9: Simulated velocity field (in m/s, see colorbar on the right) for the case 18, at t = 450 s. Colors correspond to the velocity modulus and the arrows present the velocity vectors, axes are in m.

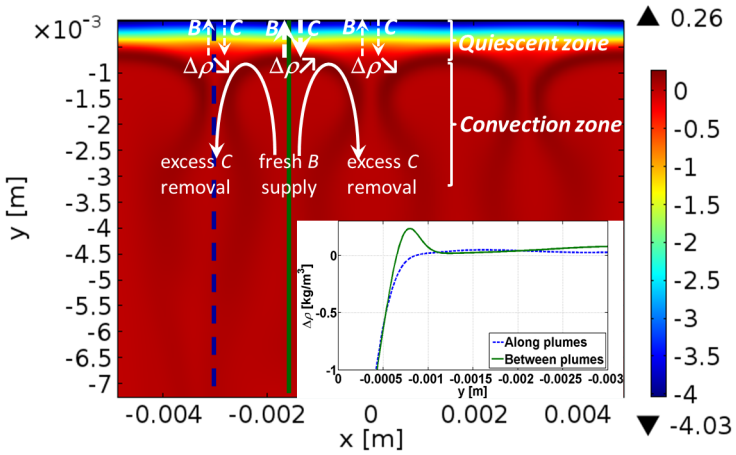

Fig. 10: Simulated DV fields (in kg/m^3, see colorbar on the right, axes in m) for case 18, after the instability onset, with a sketch of the diffusive fluxes of B and C (dashed lines) and their convective fluxes (solid lines). Inset: DV along two vertical lines (one along a plume and one between two plumes).

This is the preprint version of a manuscript accepted in Chemical Engineering Science
Permalink: http://dx.doi.org/10.1016/j.ces.2016.04.061

The transfer processes inducing the DV bump are thus amplified between the plumes in the stagnant layer. On the other hand, along the plumes, the descending liquid conveys unreacted B and some of the C produced at the interface vicinity. The excess of density is diluted in the mixed zone by the descending liquid. Therefore, the crucial phenomenon seems to be the coupling between the convective and diffusive mass transports of B and C between the stagnant and the mixed liquid, which makes their concentration in such proportion that the maximum DV tends to be softened in the descending liquid zone while it tends to be increased in the ascending liquid zone. The zones where the DV becomes maximum are thus located just in the middle of the plumes, which therefore becomes the preferred location for the next generation of plumes (leading to the oscillating behavior).

4.4. Influence of the instability on the overall mass absorption rate

In order to evaluate the effect of the instability on the mass absorption rate, several situations are considered and simulated. Hereafter, $N^{drc}_{CO_2}$ (^{drc} standing for diffusion-reaction-convection) is defined as the gas-liquid transfer rate, averaged on the interface, calculated by solving Eqs. (2)-(4) and (17)-(19) with the initial conditions (5)-(7) and (23)-(25) and the boundary conditions (8)-(16) and (26)-(32) (full system). $N^{dr}_{CO_2}$ (^{dr} standing for diffusion-reaction) is defined as the gas-liquid transfer rate, averaged over the interface, calculated by solving Eqs. (2)-(4), with $u = v = 0$, with the initial conditions (5)-(7) and the boundary conditions (8)-(16). Hence, $N^{dr}_{CO_2}$ is the gas-liquid transfer rate, averaged over the surface, that would be obtained if no instability was taking place in the cell. $N^{d}_{CO_2}$ (^{d} standing for diffusion) is also defined. It is obtained considering only the diffusive flux of CO_2, thus by solving Eq. (2), with $r = u = v = 0$, with the initial conditions (5) and the boundary conditions (8), (11) and (14). $N^{d}_{CO_2}$ is thus the averaged gas-liquid transfer rate without reaction neither convection.

The time evolutions of $N^{drc}_{CO_2}$, $N^{dr}_{CO_2}$ and $N^{d}_{CO_2}$ are compared in Fig. 11 (again for a simulation of the case 18). For $t < t^{\exp}_{\text{onset}}$, $N^{drc}_{CO_2}$ and $N^{dr}_{CO_2}$ are equal since diffusion is the only mass transport mechanism. $N^{drc}_{CO_2}$ and $N^{dr}_{CO_2}$ are much larger than $N^{d}_{CO_2}$, showing that the reaction always enhances significantly the absorption rate.

Regarding the considered case, $t^{\exp}_{\text{onset}}$ is approximately equal to 4 minutes and 30 seconds. $t^{\exp}_{\text{onset}}$ is highlighted by the red vertical line in Fig. 11. After the instability onset, it is observed that $N^{drc}_{CO_2}$ and $N^{dr}_{CO_2}$ starts to differ, though only slowly. Due to the convective transport induced by the RT

This is the preprint version of a manuscript accepted in Chemical Engineering Science
Permalink: http://dx.doi.org/10.1016/j.ces.2016.04.061

instability, $N^{drc}_{CO_2}$ becomes larger than $N^{dr}_{CO_2}$ for $t > t^{exp}_{onset}$. However, the relative difference between $N^{drc}_{CO_2}$ and $N^{dr}_{CO_2}$ reaches only 8.5% at $t = 16$ min (i.e. 11 min 10 s after the instability onset). This is obviously due to the fact that, after the instability onset, an approximately 0.5 mm thick liquid zone just below the interface remains stagnant. Hence, diffusion remains the only mechanism of mass transport across this layer.

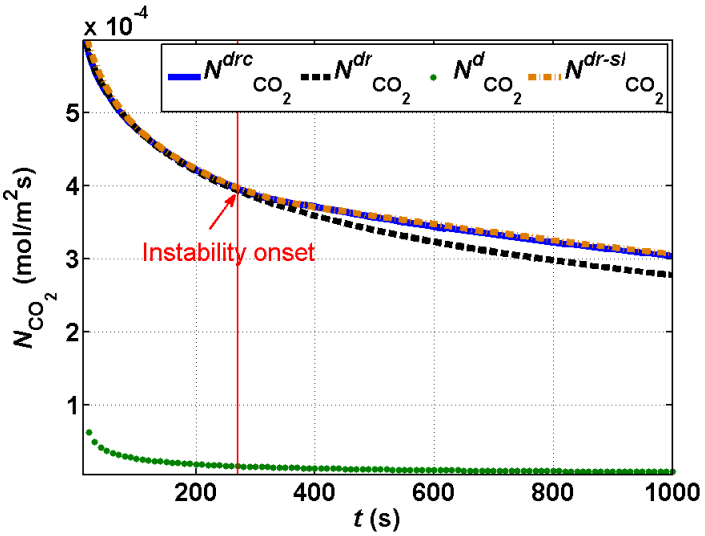

Fig. 11: Comparison of the time evolution of $N^{drc}_{CO_2}$ (solid line), $N^{dr}_{CO_2}$ (dashed line), $N^{d}_{CO_2}$ (dotted line) and $N^{d}_{CO_2}$ (dashdot line), for a simulation of the case 18. The time of the instability onset is located by the red vertical line.

This statement is evidenced by the time evolution of $N^{dr\text{-}sl}_{CO_2}$ ($^{dr\text{-}sl}$ standing for diffusion-reaction in stagnant layer), which is defined as the averaged transfer rate computed from the CO_2 flux in the stagnant layer. It is computed by solving Eqs. (2)-(4), with $u = v = 0$, with the initial conditions (5)-(7), on a shallower domain. The depth of the used domain is 0.5 mm, corresponding approximately to the thickness of the stagnant layer. The boundary conditions (8)-(10) and (14)-(16) are used but the conditions (11)-(13) (conditions at the bottom of the domain, i.e. at y = -0.5 mm) are replaced by concentration conditions, which read:

$$[CO_2]^{dr\text{-}sl}\big|_{x,\,y=-0.5\text{mm},\,t} = < [CO_2]^{drc}\big|_{x,\,y=-0.5\text{mm},\,t} > \quad (36)$$

$$[CO_3^{2-}]^{dr\text{-}sl}\big|_{x,\,y=-0.5\text{mm},\,t} = < [CO_3^{2-}]^{drc}\big|_{x,\,y=-0.5\text{mm},\,t} > \quad (37)$$

$$[HCO_3^{-}]^{dr\text{-}sl}\big|_{x,\,y=-0.5\text{mm},\,t} = < [HCO_3^{-}]^{drc}\big|_{x,\,y=-0.5\text{mm},\,t} > \quad (38)$$

This is the preprint version of a manuscript accepted in Chemical Engineering Science
Permalink: http://dx.doi.org/10.1016/j.ces.2016.04.061

$< [CO_2]^{drc}\big|_{x,\, y=-0.5\mathrm{mm},\, t} >$, $< [CO_3^{2-}]^{drc}\big|_{x,\, y=-0.5\mathrm{mm},\, t} >$ and
$< [HCO_3^-]^{drc}\big|_{x,\, y=-0.5\mathrm{mm},\, t} >$ are the CO_2, CO_3^{2-} and HCO_3^- averaged concentration along the horizontal line at y = -0.5 mm computed from the resolution of the full system.

It is observed in Fig. 11 that $N_{CO_2}^{dr\text{-}sl}$ is nearly superimposed on $N_{CO_2}^{drc}$. It shows that the transfer rate is mostly controlled by the reaction and the diffusion in the stagnant layer and by the species concentration actually reached in the zone separating the stagnant layer and the mixed zone due to the convection.

5. Conclusion and perspectives

It is shown in this paper that the particular behavior of buoyancy-induced instability observed during CO_2 absorption in aqueous solutions of $NaHCO_3$ and Na_2CO_3 inside a Hele-Shaw cell is explained by the non-monotonic shape of the DV profile before the instability onset. This DV profile presents a maximum at some distance from the interface and the plumes are generated approximately where this maximum DV is located, while the liquid close to the interface, characterized by negative DV, remains almost stagnant. A simple criterion is proposed to evaluate whether this non-monotonic shape of DV profile is expected to be met in a given system.

The numerical simulation results obtained in this work show that the model is able to reproduce the DV field evolution before the instability onset and most characteristics of the instability dynamics after its onset. This validates the assumption that this instability is triggered by a Rayleigh-Taylor mechanism. In particular, it is observed that the model provides in most cases a good estimation for the time of the onset t_{onset}, while it tends to clearly overestimates p_{onset} (hydrostatic pressure excess in the DV bump).

Besides, the simulation results confirm the presence of an almost quiescent liquid layer close to the interface. This was foreseen from the experimental observation of a rather steady homogeneous DV field in the interface vicinity after the instability onset. It is also shown that the oscillating behavior of the formed plumes results from the combination of the diffusive and convective fluxes of B and C in the liquid, generating a maximum of density between the initially formed plumes. Finally, it is demonstrated that the development of the instability does not significantly enhance the gas-liquid transfer rate, due to the particular DV field in the vicinity of the interface. This rate remains actually controlled by the diffusion in the almost quiescent layer of liquid in

This is the preprint version of a manuscript accepted in Chemical Engineering Science
Permalink: http://dx.doi.org/10.1016/j.ces.2016.04.061

contact with the interface and having a thickness of the order of one mm. The convective mixing of the liquid due to the instability takes place below this layer. This clearly illustrates that buoyancy-induced RT instability does not systematically enhance the absorption rate significantly, contrary to what is commonly expected. These results could be of significant importance for the design and the optimization of processes involving chemi-sorption.

Despite the relatively good agreement between experiments and simulations, the two-dimensional model presented in this paper might be not complete enough to capture all the phenomena taking place during the development of the Rayleigh-Taylor instability, especially as far as the long term evolution is concerned. Notably, simulations of a three-dimensional model, taking into account the meniscus shape of the interface inside the Hele-Shaw, would very likely provide better comparisons with experiments.

Acknowledgements

The authors are thankful to Prof. A. De Wit and her team for helpful discussions. The postdoctoral researcher Christophe Wylock and the F.R.S.-FNRS (Belgian National Fund for Scientific Research) senior research associate Pierre Colinet gratefully acknowledge the financial support from the Fund. The authors also acknowledge financial support of the Belgian Science Policy (BELSPO) and European Space Agency (ESA) via the PRODEX programme. This study is also related to the activity of the European COST action MP1106 "Smart and green interfaces - from single bubbles and drops to industrial, environmental and biomedical applications".

A. Operating parameters and reaction modelling

A.1. Reactions when CO_2 *is transferred in an aqueous solution of* $NaHCO_3$ *and* Na_2CO_3

It is well known that the CO_2 dissolved in aqueous solutions of $NaHCO_3$ and Na_2CO_3 takes part to the following two chemical reactions (Danckwerts, 1970; Danckwerts and Kennedy, 1958; Rhem et al., 1963; Vas Bhat et al., 2000; Cents et al., 2005):

$$CO_2 + OH^- \rightleftharpoons HCO_3^- \tag{39}$$

$$HCO_3^- + OH^- \rightleftharpoons CO_3^{2-} + H_2O \tag{40}$$

Let $K_1 = \frac{[HCO_3^-]}{[CO_2][OH^-]}$ and $K_2 = \frac{[CO_3^{2-}]}{[HCO_3^-][OH^-]}$ be their respective equilibrium constants and let k_1 and k_2 be their respective kinetic constants. Simplifications of the chemical reaction scheme can be realized, as presented by Danckwerts (1970). Indeed, according to the correlations presented in Vas Bhat et al. (2000) and Cents et al. (2005) to estimate the numerical values of k_1, k_2, K_1 and K_2, it is found that K_1 is high enough (about $4\,10^5$ m^3/mol) to consider that the first reaction is irreversible and that k_2 is high enough to consider that the second reaction is instantaneously at equilibrium. In addition, the value of K_2 is such that the consumption of one mole of CO_2 (by the first reaction) leads to the consumption of one mole of CO_3^{2-} (by the inverse of the second reaction) and, globally, to the production of two moles of HCO_3^-, the concentration of OH^- remaining almost constant. At equilibrium, the concentrations of CO_2 and OH^- are approximately four orders of magnitude smaller than the HCO_3^- and the CO_3^{2-} concentrations. Therefore, the chemical reaction scheme can be reduced to only one global irreversible reaction, which writes:

$$CO_2 + CO_3^{2-} + H_2O \rightarrow 2HCO_3^- \tag{41}$$

The limiting step of the rate of this global reaction is the reaction between CO_2 and OH^-. Thus the reaction rate is given by $k_1[CO_2][OH^-]$. Since the OH^- concentration can be evaluated from the HCO_3^- and CO_3^{2-} concentrations and the equilibrium constant K_2 by $[OH^-] = [CO_3^{2-}]/K_2[HCO_3^-]$, the global chemical reaction rate can then by estimated by:

$$r = k_1[CO_2]\frac{[CO_3^{2-}]}{K_2[HCO_3^-]} \tag{42}$$

Concerning the density variations modelling, the density of $NaHCO_3$-Na_2CO_3 aqueous solutions has been investigated experimentally in a previous work (Wylock et al., 2011) for various $NaHCO_3$ and Na_2CO_3 concentrations. It has been determined that the density varies almost linearly with the HCO_3^- and CO_3^{2-} concentrations. The density variation induced by the CO_2 OH^- concentration variations is negligible. The following expression has thus been proposed to estimate the liquid DV in the Hele-Shaw cell during the CO_2 absorption:

$$\Delta\rho|_{x,y,t} = \left.\frac{\partial\rho}{\partial[CO_3^{2-}]}\right|_{[CO_3^{2-}]_0,[HCO_3^-]_0} \Delta[CO_3^{2-}]\big|_{x,y,t} + \left.\frac{\partial\rho}{\partial[HCO_3^-]}\right|_{[CO_3^{2-}]_0,[HCO_3^-]_0} \Delta[HCO_3^-]\big|_{x,y,t} \tag{43}$$

This is the preprint version of a manuscript accepted in Chemical Engineering Science
Permalink: http://dx.doi.org/10.1016/j.ces.2016.04.061

where $\frac{\partial \rho}{\partial [CO_3^{2-}]}$ and $\frac{\partial \rho}{\partial [HCO_3^-]}$ (in kg/mol) are the partial derivatives of the density with respect to the CO_3^{2-} and HCO_3^- concentrations, respectively, and where $\Delta[CO_3^{2-}]\big|_{x,y,t} = \left([CO_3^{2-}]\big|_{x,y,t} - [CO_3^{2-}]_0 \right)$ and $\Delta[HCO_3^-]\big|_{x,y,t} = \left([HCO_3^-]\big|_{x,y,t} - [HCO_3^-]_0 \right)$. $[CO_3^{2-}]_0$ and $[HCO_3^-]_0$ are the initial concentrations in CO_3^{2-} and HCO_3^-, respectively.

A.2. Physicochemical parameters used in the simulations

The density ρ and the viscosity μ of the aqueous solution are functions of the solution composition. They are calculated from experimental correlations provided by Solvay s.a. that are not allowed to be reproduced here.

According to the results presented in (Wylock et al., 2011), D_{CO_2} and K_1 are well estimated by correlations from the literature.

D_{CO_2} is estimated by (Pohorecki and Moniuk, 1988):

$$D_{CO_2} = D_{CO_2,w} \frac{\mu_w}{\mu} \tag{44}$$

where μ_w and $D_{CO_2,w}$ are the viscosity of pure water and the CO_2 diffusion coefficient in pure water, respectively. $D_{CO_2,w}$, is calculated by:

$$\log D_{CO_2,w} = -8.1764 + \frac{712.52}{T} - \frac{259070}{T^2} \tag{45}$$

K_1 is considered to depend only on the temperature. It is calculated by (Edwards et al., 1978):

$$K_1 = \frac{1}{K_w} \exp\left(\frac{-12092.1}{T} - 36.786 \ln(T) + 235.482 \right) \rho_w \tag{46}$$

where ρ_w is the density of pure water and K_w is the ionic product of water. K_w is calculated by (Vas Bhat et al., 2000):

$$K_w = 10^{-\left(\frac{5839.5}{T} + 22.4773 \log(T) - 61.2062\right)} \rho_w^2 \tag{47}$$

The value of K_1 is $42627 \mathrm{m}^3/\mathrm{mol}$.

Concerning the numerical values of the other parameters $D_{HCO_3^-}$, $D_{CO_3^{2-}}$, k_1, K_2, $\frac{\partial \rho}{\partial [HCO_3^-]}$, $\frac{\partial \rho}{\partial [CO_3^{2-}]}$ and h, it has been shown in a previous work that literature and experimental correlations are not accurate enough to reproduce the experimentally determined liquid DV profile time evolution before

This is the preprint version of a manuscript accepted in Chemical Engineering Science
Permalink: http://dx.doi.org/10.1016/j.ces.2016.04.061

the instability onset (Wylock et al., 2011). A non-linear least-square parametric estimation had then been realized to fit these parameters from the experimentally observed DV profiles (before the instability onset). The fitted parameter values are presented in Table 2, for the various couples of $NaHCO_3$ and Na_2CO_3 concentrations identified by their case number (see Table 1).

This is the preprint version of a manuscript accepted in Chemical Engineering Science
Permalink: http://dx.doi.org/10.1016/j.ces.2016.04.061

N°	ρ $\left(\frac{\text{kg}}{\text{m}^3}\right)$	μ $\left(10^{-3}\ \frac{\text{kg}}{\text{m s}}\right)$	D_{CO_2} $\left(10^{-10}\ \frac{\text{m}^2}{\text{s}}\right)$	$D_{HCO_3^-}$ $\left(10^{-10}\ \frac{\text{m}^2}{\text{s}}\right)$	$D_{CO_3^{2-}}$ $\left(10^{-10}\ \frac{\text{m}^2}{\text{s}}\right)$	k_1 $\left(\frac{\text{m}^3}{\text{mol s}}\right)$	K_2 $\left(\frac{\text{m}^3}{\text{mol}}\right)$	$\frac{\partial\rho}{\partial[HCO_3^-]}$ $\left(10^{-2}\frac{\text{kg}}{\text{mol}}\right)$	$\frac{\partial\rho}{\partial[CO_3^{2-}]}$ $\left(10^{-2}\frac{\text{kg}}{\text{mol}}\right)$	h $(-)$
1	1033	1.00	17.7	8.9	7.7	10.22	5.37	5.02	10.24	0.631
2	1053	1.10	16.1	11.0	10.5	11.18	5.17	5.12	10.27	0.531
3	1074	1.23	15.7	3.7	3.4	10.71	4.38	5.66	11.77	0.505
4	1095	1.40	12.7	7.7	7.2	15.12	5.20	5.44	10.91	0.370
5	1116	1.60	11.0	6.9	6.5	17.75	5.31	5.00	10.14	0.313
6	1137	1.86	9.5	6.1	5.8	20.85	5.18	5.07	10.32	0.249
7	1159	2.18	8.1	6.2	5.8	24.66	5.72	4.92	9.99	0.199
8	1181	2.58	6.9	5.1	4.3	29.18	5.34	5.03	10.49	0.152
9	1048	1.06	16.7	11.2	10.4	9.54	5.42	5.18	10.38	0.554
10	1068	1.16	15.2	10.6	10.0	11.99	5.19	5.10	10.27	0.461
11	1089	1.30	13.6	9.6	9.2	13.66	5.56	5.38	10.77	0.356
12	1110	1.48	12.0	7.6	7.2	15.91	5.31	5.06	10.23	0.325
13	1131	1.70	10.4	7.5	7.0	18.58	5.85	4.84	9.75	0.255
14	1152	1.97	9.0	6.6	6.0	21.93	5.54	4.98	10.08	0.208
15	1174	2.31	7.6	6.0	5.4	25.81	5.51	5.04	10.37	0.158
16	1062	1.12	15.8	9.2	8.1	10.20	4.85	5.26	10.46	0.493
17	1083	1.23	14.3	3.9	3.7	11.62	4.03	6.37	12.95	0.427
18	1104	1.38	12.8	7.5	6.9	13.88	5.14	5.30	10.69	0.337

Table 2: Concentrations and corresponding physicochemical parameters of the studied solutions (Wylock et al., 2011).

B. 1D modelling of the DV profile

Considering that the reaction $CO_2 + \nu_B\, B \rightarrow \nu_C\, C$ is fast enough compared to the species transport, this reaction can be considered as confined to a thin liquid layer at the interface, beyond which the dissolved CO_2 is almost depleted. Therefore, the reaction scheme can be simplified by considering the reaction as instantaneous and taking place only at the gas-liquid interface. It is a reasonable assumption in our case, the actual reaction zone being much thinner than the diffusive boundary layer at the instability onset.

Due to the instantaneous character of the reaction, the CO_2 does not penetrate in the liquid, B is totally depleted at the interface and thus there is no reaction in the liquid. This reduces the system to two diffusive transport equations. In such a case, the transport will take place only along the vertical direction, leading to one-dimensional expression. The equations write therefore:

$$\frac{\partial [B]}{\partial t} = D_B \frac{\partial^2 [B]}{\partial y^2} \tag{48}$$

$$\frac{\partial [C]}{\partial t} = D_C \frac{\partial^2 [C]}{\partial y^2} \tag{49}$$

Far from the interface ($y \rightarrow -\infty$), it is considered that the concentrations of B and C are equal to the initial (i.e. at $t = 0$) bulk concentrations, leading to:

$$\lim_{y \rightarrow -\infty} [B](t, y) = [B](t = 0, y) = [B]_0 \tag{50}$$

$$\lim_{y \rightarrow -\infty} [C](t, y) = [C](t = 0, y) = [C]_0 \tag{51}$$

At the interface (i.e. $y = 0$), the complete depletion of B and a production of C equal to the consumption of B are considered, leading to:

$$[B](t, y = 0) = 0 \tag{52}$$

$$D_C \left. \frac{\partial [C]}{\partial y} \right|_{t, y=0} = -\frac{\nu_C}{\nu_B} D_B \left. \frac{\partial [B]}{\partial y} \right|_{t, y=0} \tag{53}$$

Eqs. (48) and (49) can be solved analytically using the conditions given by Eqs. (50)-(53). Their solution reads:

$$[B](t, y) = [B]_0 \left(1 - \operatorname{erfc} \left(\frac{-y}{2\sqrt{D_B t}} \right) \right) \tag{54}$$

$$[C](t, y) = [C]_0 + \frac{\nu_C}{\nu_B} \sqrt{\frac{D_B}{D_C}}\, [B]_0 \operatorname{erfc} \left(\frac{-y}{2\sqrt{D_C t}} \right) \tag{55}$$

This is the preprint version of a manuscript accepted in Chemical Engineering Science
Permalink: http://dx.doi.org/10.1016/j.ces.2016.04.061

By injecting Eqs.(54) and (55) in the one-dimensional form of Eq. (20), the following expression is obtained to estimate the DV profile along the depth, before the instability onset:

$$\Delta\rho(t,y) = \frac{\partial\rho}{\partial[C]}[B]_0\frac{\nu_C}{\nu_B}\sqrt{\frac{D_B}{D_C}}\mathrm{erfc}\left(\frac{-y}{2\sqrt{D_C t}}\right) - \frac{\partial\rho}{\partial[B]}[B]_0\,\mathrm{erfc}\left(\frac{-y}{2\sqrt{D_B t}}\right) \tag{56}$$

It can be seen that the solution given by Eq. (56) is self-similar and that its shape depends only on two ratios. $[C]_0$ has no influence on the DV profile and $[B]_0$ influences only its amplitude. The following dimensionless expressions are defined: $\tilde{D} = D_C/D_B$, $\tilde{\nu} = \nu_C/\nu_B$, $\tilde{\delta} = \frac{\partial\rho}{\partial[C]}/\frac{\partial\rho}{\partial[B]}$ and $\tilde{y} = -y/2\sqrt{D_B t}$. The dimensionless DV shape $\widetilde{\Delta\rho} = \Delta\rho/\frac{\partial\rho}{\partial[B]}[B]_0$ is deduced from Eq. (56) and reads:

$$\widetilde{\Delta\rho}(\tilde{y}) = \frac{\tilde{\nu}\,\tilde{\delta}}{\sqrt{\tilde{D}}}\mathrm{erfc}\left(\frac{\tilde{y}}{\sqrt{\tilde{D}}}\right) - \mathrm{erfc}\,(\tilde{y}) \tag{57}$$

It shows that the DV profile shape depends only on $\tilde{D}$ and $\tilde{\nu}\,\tilde{\delta}$.

On the one hand, the DV at interface is positive if $\tilde{\nu}\,\tilde{\delta} > \sqrt{\tilde{D}}$, zero if $\tilde{\nu}\,\tilde{\delta} = \sqrt{\tilde{D}}$ and negative if $\tilde{\nu}\,\tilde{\delta} < \sqrt{\tilde{D}}$. On the other hand, the first derivative of Eq. (57) with respect to $\tilde{y}$ is zero if:

$$\tilde{y} = -\sqrt{\frac{\tilde{D}}{\tilde{D}-1}\log\left(\frac{\tilde{D}}{\tilde{\nu}\,\tilde{\delta}}\right)} \tag{58}$$

The DV profile presents an extremum (i.e. it is non-monotonic) for values of $\tilde{D}$ and $\tilde{\nu}\tilde{\delta}$ such that $\tilde{y}$ is real. This extremum is a minimum if $\tilde{D} < 1$ and $\tilde{\nu}\,\tilde{\delta} \geq \tilde{D}$ and a maximum if $\tilde{D} > 1$ and $\tilde{\nu}\,\tilde{\delta} \leq \tilde{D}$.

A classification of the various DV profile shapes described by Eq. (57) is presented in Fig. 12, which displays some representative DV profiles. In particular, it is shown that the non-monotonic DV profiles observed in aqueous solutions of $NaHCO_3$ and Na_2CO_3 occur when $\tilde{D} > 1$ and $\tilde{\nu}\,\tilde{\delta} < \sqrt{\tilde{D}}$.

This is the preprint version of a manuscript accepted in Chemical Engineering Science
Permalink: http://dx.doi.org/10.1016/j.ces.2016.04.061

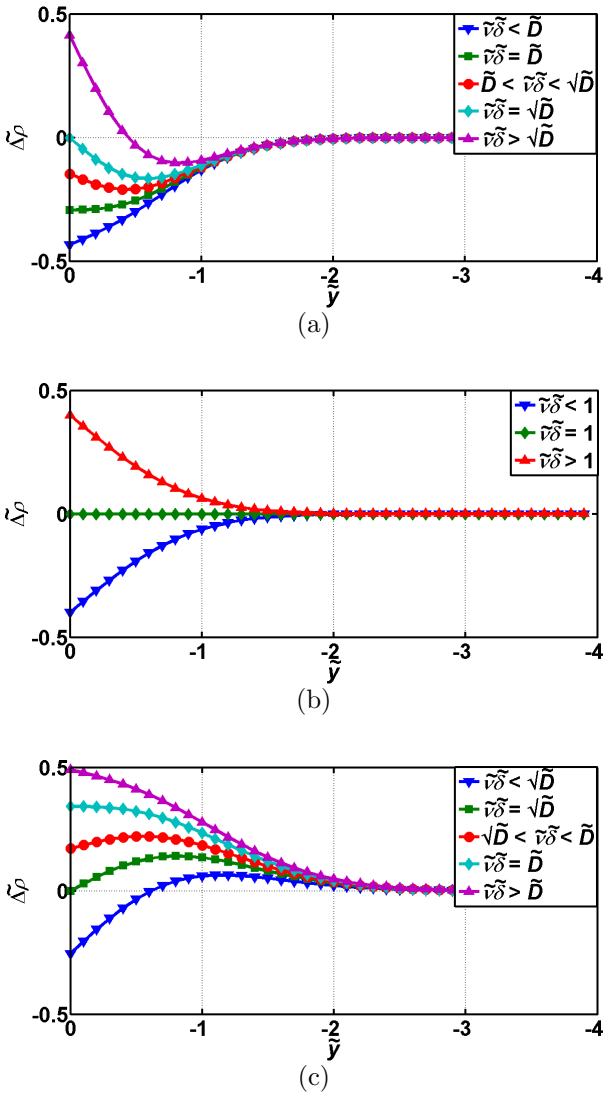

Fig. 12: Dimensionless DV profiles for $\tilde{D} < 1$ (a), $\tilde{D} = 1$ (b) and $\tilde{D} > 1$ (c). They are obtained from Eq. (57).

This is the preprint version of a manuscript accepted in Chemical Engineering Science
Permalink: http://dx.doi.org/10.1016/j.ces.2016.04.061

Nomenclature

Latin

$[X]$	concentration of species X, mol/m^3
d	computational domain depth, m
D	diffusion coefficient, m^2/s
$\tilde{D}$	ratio of the diffusion coefficient of C to the diffusion coefficient of B
DV	density variation
e	distance between the two parallel plates of the Hele-Shaw cell, m
g	gravity acceleration, m/s^2
h	solubility coefficient
k	kinetic constant
K	equilibrium constant
MZI	Mach-Zehnder interferometer
N	averaged interfacial gas-liquid transfer rate, mol/(m^{2}s)
NSD	Navier-Stokes-Darcy
p	pressure, Pa
r	reaction rate, mol/(m^{3}s)
R	ideal gas constant, J/(mol K)
RI	refractive index
RT	Rayleigh-Taylor
t	time, s
T	absolute temperature, K
u	horizontal component of the velocity, m/s
v	vertical component of the velocity, m/s
w	computational domain width, m
x	horizontal coordinate, m
y	vertical coordinate, m
$\tilde{y}$	dimensionless vertical coordinate

Greek

$\tilde{\delta}$	ratio of the density contribution of C to the density contribution of B
Δ	variation
μ	dynamic viscosity, kg/(m s)
ν	stoichiometric coefficient
$\tilde{\nu}$	ratio of the stoichiometric coefficient of C to the stoichiometric coefficient of B
ρ	density, kg/m^3

This is the preprint version of a manuscript accepted in Chemical Engineering Science
Permalink: http://dx.doi.org/10.1016/j.ces.2016.04.061

Superscript

d	diffusion case
dr	diffusion-reaction case
drc	diffusion-reaction-convection case
$dr\text{-}sl$	diffusion reaction in stagnant layer case
exp	experimental
sim	simulated

Subscript

0	at initial time
onset	at instability onset
w	water

References

Bird, R., Stewart, W., Lightfoot, E., 2002. Transport Phenomena. John Wiley&Sons, New York.

Cents, A., Brilman, D., Versteeg, G., 2005. CO_2 absorption in carbonate/bicarbonate solutions: The danckwerts-criterion revisited. Chemical Engineering Science 60, 5830–5835.

Coulson, J., Richardson, J., 1999. Chemical Engineering Vol. 1 : Fluid flow, heat transfer and mass transfer, 6th Edition. Butterworth Heinemann.

Danckwerts, P., 1970. Gas-Liquid Reactions. Chemical Engineering Series. McGraw-Hill.

Danckwerts, P., Kennedy, A., 1958. The kinetics of absorption of carbon dioxide into neutral and alkaline solutions. Chemical Engineering Science 8, 201–215.

Edwards, T., Maurer, G., Newman, J., Prausnitz, J., 1978. Vapor-liquid equilibria in multicomponent aqueous solutions of volatile weak electrolytes. AIChE Journal 24 (6), 966–976.

Gondret, P., Rabaud, M., 1997. Shear instability of two-fluid parallel flow in a Hele-Shaw cell. Physics of Fluids 9 (11), 3267–3274.

Harvey, E., Smith, W., 1959. The absorption of carbon dioxide by a quiescent liquid. Chemical Engineering Science 10, 274–280.

Javaheri, M., Abedi, J., Hassanzadeh, H., 2010. Linear stability analysis of double-diffusive convection in porous media, with application to geological storage of CO_2. Transp. Porous Med. 84(2), 441–456.

Kim, M., 2015. Linear and nonlinear analyses on the onset of gravitational instabilities in a fluid saturated within a hele-shaw cell. Chemical Engineering Science 126, 349.

Kim, M., Choi, C., 2012. Linear stability analysis on the onset of buoyancy-driven convection in liquid-saturated porous medium. Physics of Fluids 24, 044102.

Loodts, V., Rongy, L., De Wit, A. . 2014, . ., 2014a. Impact of pressure, salt concentration, and temperature on the convective dissolution of carbon dioxide in aqueous solutions. Chaos 24, 043120.

Loodts, V., Thomas, C., Rongy, L., De Wit, A., 2014b. Control of convective dissolution by chemical reactions: General classification and application to CO_2 dissolution in reactive aqueous solutions. Physical Review Letters 113, 114501.

Martin, J., Rakotomalala, N., Salin, D., 2002. Gravitational instability of miscible fluids in a hele-shaw cell. Physics of Fluids 14 (2), 902–905.

Pohorecki, R., Moniuk, W., 1988. Kinetics of reaction between carbon dioxide and hydroxyl ions in aqueous electrolyte solutions. Chemical Engineering Science 43, 1677–1684.

Rhem, T. R., Moll, A. J., Babb, A. L., Novembre 1963. Unsteady state absorption of carbon dioxide by dilute sodium hydroxyde solutions. AIChE Journal 9 (6), 760–765.

Riaz, A., Hesse, M., Tchelepi, H., Orr, F., 2006. Onset of convection in a gravitationally unstable diffusive boundary layer in porous media. Journal of Fluid Mechanics 548, 87–111.

Rongy, L., Haugen, K., Firoozabadi, A., 2012. Mixing from Fickian diffusion and natural convection in binary non-equilibrium fluid phases. AIChE Journal 58, 1336–1345.

This is the preprint version of a manuscript accepted in Chemical Engineering Science
Permalink: http://dx.doi.org/10.1016/j.ces.2016.04.061

Ruyer-Quil, C., 2001. Inertial corrections to the Darcy law in a Hele-Shaw cell. C. R. Acad. Sci. Paris IIB Mech. 329(5), 337–342.

Trambouze, P., Euzen, J.-P., 2004. Chemical Reactors: from design to operation. Institut Français du pétrole Publications. Technip.

Vas Bhat, R., Kuipers, J., Versteeg, G., 2000. Mass transfer with complex chemical reactions in gas-liquid systems: two-step reversible reactions with unit stoichiometric and kinetic orders. Chemical Engineering Journal 76, 127–152.

Wylock, C., Dehaeck, S., Cartage, T., Colinet, P., Haut, B., 2011. Experimental study of gas-liquid mass transfer coupled with chemical reactions by digital holographic interferometry. Chemical Engineering Science 66(14), 3400–3412.

Wylock, C., Dehaeck, S., Quintans, D., Colinet, P., Haut, B., 2013. CO_2 absorption in aqueous solutions of N-(2-hydroxyethyl)piperazine: Experimental characterization using interferometry and modeling. Chemical Engineering Science 100, 249–258.

Wylock, C., Dehaeck, S., Rednikov, A., Colinet, P., 2008. Chemo-hydrodynamic instability generated by CO_2 absorption in an aqueous solution of $NaHCO_3$ and Na_2CO_3. Microgravity Science and Technology 20, 171–175.

Wylock, C., Rednikov, A., Haut, B., Colinet, P., 2014. Nonmonotonic Rayleigh-Taylor instabilities driven by gas-liquid CO_2 chemisorption. Journal of Physical Chemistry B 118, 11323–11329.